

ARTICLE

Open Access

An Optoelectronic thermometer based on microscale infrared-to-visible conversion devices

He Ding¹✉, Guoqing Lv¹, Xue Cai², Junyu Chen², Ziyi Cheng¹, Yanxiu Peng¹, Guo Tang², Zhao Shi², Yang Xie², Xin Fu³, Lan Yin³, Jian Yang¹, Yongtian Wang¹ and Xing Sheng²✉

Abstract

Thermometric detectors are crucial in evaluating the condition of target objects spanning from environments to the human body. Optical-based thermal sensing tools have received extensive attention, in which the photon upconversion process with low autofluorescence and high tissue penetration depth is considered as a competent method for temperature monitoring, particularly in biomedical fields. Here, we present an optoelectronic thermometer via infrared-to-visible upconversion, accomplished by integrated light receiving and emission devices. Fully fabricated thin-film, microscale devices present temperature-dependent light emission with an intensity change of $1.5\% ^\circ\text{C}^{-1}$ and a spectral shift of $0.18 \text{ nm } ^\circ\text{C}^{-1}$. The sensing mechanism is systematically characterized and ascribed to temperature dependent optoelectronic properties of the semiconductor band structure and the circuit operation condition. Patterned device arrays showcase the capability for spatially resolved temperature mapping. Finally, in vitro and in vivo experiments implemented with integrated fiber-optic sensors demonstrate real-time thermal detection of dynamic human activity and in the deep brain of animals, respectively.

Introduction

Spatially and temporally resolved temperature sensing with high precision is critically important and has wide applications in diverse fields, such as industrial manufacturing, environmental, and healthcare monitoring^{1–5}. Specifically, real-time detection of temperature variations in biological systems is essential for point-of-care diagnostics and treatment^{5–7}. Point contact temperature monitoring is commonly based on thermoelectric or thermoresistive sensors, but such wired electrical designs usually incorporate metallic embodiments that are easily intervened by electromagnetic waves, particularly during

magnetic resonance imaging (MRI)^{1,8}. On the other hand, optical-based sensors offer attractive solutions in temperature monitoring for biomedical diagnosis, owing to their remote detection, minimal invasion, immunity to electromagnetic interferences, and high resolution^{1,9–13}. These optical sensing modalities can be based on the luminescence intensity, wavelength, peak width, and/or decay lifetime^{1,11,12}. Infrared thermometers and imagers capture spatially resolved temperature information in a non-contact mode by collecting blackbody radiation emitted from the targeting object, but the devices only detect surface temperatures, and the results are highly influenced by surface emissivity^{13,14}. Thermal sensors based on optical cavities exhibit spectrally resolved optical responses with very high precision^{3,8}, but their measurements usually rely on sophisticated spectrometric systems in stable fixtures that could limit their biomedical applications. Phase changing materials like liquid crystals also present temperature-dependent color changes, but their perceived color can be limited by the environment lighting, viewing angles, polarizations, etc^{15–17}.

Correspondence: He Ding (heding@bit.edu.cn) or Xing Sheng (xingsheng@tsinghua.edu.cn)

¹Beijing Engineering Research Center of Mixed Reality and Advanced Display, School of Optics and Photonics, Beijing Institute of Technology, Beijing 100081, China

²Department of Electronic Engineering, Beijing National Research Center for Information Science and Technology, Institute for Precision Medicine, Center for Flexible Electronics Technology, and IDG/McGovern Institute for Brain Research, Tsinghua University, Beijing 100084, China

Full list of author information is available at the end of the article

© The Author(s) 2022



Open Access This article is licensed under a Creative Commons Attribution 4.0 International License, which permits use, sharing, adaptation, distribution and reproduction in any medium or format, as long as you give appropriate credit to the original author(s) and the source, provide a link to the Creative Commons license, and indicate if changes were made. The images or other third party material in this article are included in the article's Creative Commons license, unless indicated otherwise in a credit line to the material. If material is not included in the article's Creative Commons license and your intended use is not permitted by statutory regulation or exceeds the permitted use, you will need to obtain permission directly from the copyright holder. To view a copy of this license, visit <http://creativecommons.org/licenses/by/4.0/>.

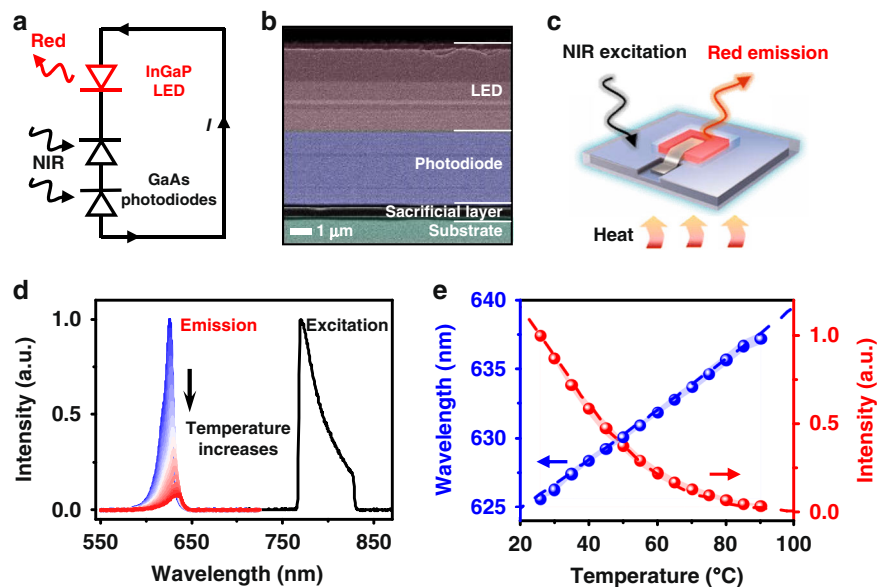


Fig. 1 An optoelectronic upconversion device with temperature dependent light emission. **a** Circuit diagram and **(b)** Scanning electron microscopic (SEM) image of the optoelectronic upconversion design, including an InGaP red LED and a GaAs double junction photodiode with serial connection. **c** Schematic diagram of the upconversion device for temperature sensing. **d** Spectra of the excitation and the upconverted photoluminescence (PL) emission at varied temperatures (25–90 °C). **e** Calculated (dash line) and measured (dots) peak wavelength and PL intensity of the upconverted red emission as a function of temperature, and the shaded range represents the standard deviation measured among 10 samples

Alternatively, temperature readout can be aided by the deployment of photoluminescent (PL) materials or devices, with the thermal status influencing their emission intensity, peak wavelength, decay lifetime, etc.^{9–12,18–20}. These thermally dependent luminescent sensors provide visualized temperature information with a high spatio-temporal resolution, offering tremendous advantages and opportunities in areas like bioimaging^{9–12,20,21}. While the temperature-dependent PL mechanism via the down-conversion process requires a short-wavelength excitation, upconversion processes that transform near-infrared (NIR) photons in the range of the biological transparency window (around 650–950 nm) to visible ones are more advantageous and have emerged as an area of interest, particularly for biomedical applications^{9,11,22–27}. Compared to the downconversion counterpart, such an upconversion mechanism mitigates the biological autofluorescence, facilitates tissue penetration, and yields conveniently-visualized and easily-captured visible light signals, presenting a more suitable method for sensing in biological systems^{9,11,23–26,28}. As a representative and the most commonly used upconversion material, lanthanide-based nanoparticles leverage the PL emissions from two or more independent bands that exhibit strong temperature dependence, which have been applied for thermal sensing in biomedicine^{19,23,25,29}. Recently, optoelectronic NIR-to-visible upconversion devices based on designed semiconductor heterostructures have been developed, exhibiting a linear response, fast dynamics, and low excitation

power^{30–32}. As a microscale device that can be implanted into the animal body, such an optoelectronic design shows promise for various optical sensing applications.

In this study, we systematically investigated temperature-dependent PL characteristics of the optoelectronic upconversion device and demonstrated its capability for thermal sensing. We discovered that its thermal-dependent PL emission is determined by the band properties of semiconductor materials as well as the integrated device circuit architecture. Arrays of patterned devices present spatially resolved temperature mapping in ambient environments. Furthermore, microscale devices integrated with fiber optics are employed for in vitro and in vivo applications, dynamically monitoring human exhalation activities and temperature variations in the deep brain of behaving animals.

Results

The proposed temperature sensing strategy is based on a fully integrated optoelectronic upconversion device schematically shown in Fig. 1a, consisting of a low-bandgap, gallium arsenide (GaAs) based double junction photodiode and a large-bandgap, indium gallium phosphide (InGaP) based light-emitting diode (LED) connected in series, with the band structure in Fig. S1. Figure 1b displays the cross-sectional scanning electron microscope (SEM) image of the device structure, which was grown on the GaAs substrate with a sacrificial interlayer. As demonstrated previously, the lithographically defined and epitaxially released microscale devices (size $\sim 300 \times 300 \mu\text{m}^2$) realize efficient NIR-to-visible

upconversion with a linear response and ultrafast dynamics (Fig. 1c)^{31,32}. In particular, here we find that the devices' PL emission exhibit strong temperature dependence. Figure 1d depicts the spectroscopic performance of the device under steady-state NIR excitation at a wavelength range of 770–830 nm (power density $\sim 40 \text{ mW cm}^{-2}$, without causing additional photothermal effects in the tissue, as shown in Fig. S2)³³, with red emission recorded by a fluorescence microscope equipped spectrometer (details in Fig. S3). Potentially used in the biomedical field, a temperature range from room temperature ($\sim 25^\circ\text{C}$) to 90°C is selected, in which the compositional materials (III–V semiconductors, encapsulants, and metal electrodes) in the device are stable. When the device temperature increases, the PL intensity decreases, accompanied by a redshift with the emission peak increasing from 625 nm to 637 nm. Device performance collected from 10 different devices is presented in Fig. 1e and S5. The measurements indicate an intensity-temperature sensitivity of $\sim 1.5\% ^\circ\text{C}^{-1}$ and a spectrum-temperature sensitivity of $\sim 0.18 \text{ nm } ^\circ\text{C}^{-1}$. Here the intensity-temperature sensitivity is subjected to the relative intensity, as the collected PL intensity is dependent on various factors, including the excitation power, efficiency of the spectrometer, device geometry, etc. On the other hand, the temperature-dependent spectral peak shift is subjected to the absolute sensitivity, in which the emission peak wavelength of the device depends on the bandgap of the InGaP semiconductor, regardless of other external factors. These experimental results are in quantitative accordance with theoretical calculations based on the detailed balance model for diodes and the empirical Varshni expression on the relationship between bandgap energy and temperature (see Supplementary Information for detailed calculations)^{34–36}. We further analyze the noise associated with the spectral reading in Figure S6. Recorded at 27°C , 48°C , 65°C , and 90°C averaged signal-to-noise ratios (SNR) in the peak wavelength range ($\pm 5 \text{ nm}$) is above 15, larger than the 3 dB boundary. Taking the standard deviation of the normalized intensity at these representative temperatures, calculated temperature resolutions are 0.01°C , 0.06°C , 0.14°C , and 0.49°C , respectively. Similarly, resolutions of 0.04°C , 0.08°C , 0.11°C , and 0.22°C are achieved based on the peak wavelength shift at these representative temperatures.

To further grasp the thermal sensing mechanism of the upconversion device, we analyze the properties of individual electronic components with the device structure. We fabricate microscale InGaP LEDs (Fig. 2a) and GaAs photodiodes (Fig. 2d) and evaluate their thermal behaviors, separately. These individual devices have the same epitaxial structures as those in the upconversion device and are lithographically patterned to form similar microscale geometries^{31,32,37}. The temperature-dependent electroluminescent (EL) spectra of the InGaP LED (Fig. 2b, c) are similar to those measured in the upconversion device

(Fig. 1d, e). First, the EL peak shift coincides with that of the upconversion device, since the peak wavelength is mostly associated with the bandgap of the InGaP semiconductor (Fig. S4). Second, the LED emission intensity also decreases at elevated temperatures; however, the intensity-temperature relative sensitivity ($\sim 1.2\% ^\circ\text{C}^{-1}$) is lower than that of the upconversion device, because the upconverted PL intensity is defined by both the LED and the photodiode. Compared with the LED powered by a stable external current source, the LED in the upconversion device is powered by the GaAs photodiode with temperature-dependent efficiencies, which further reduces the PL output at elevated temperatures. Figure 2e plots the external quantum efficiency (EQE) spectra of the double junction GaAs photodiode. When temperature increases, the optical absorption edge exhibits a redshift due to the narrowed bandgap of GaAs. Additionally, the EQE maximum decreases and the spectral peak slightly moves to longer wavelengths (Fig. 2f), which can be ascribed to the photocurrent mismatch within the double junction photodiode at elevated temperatures. Figure 2g summarizes the efficiency drops for all the devices (LED, photodiode, and the upconversion device). These results reveal that the intensity-temperature dependence of the upconversion device is determined by the efficiency drops of both the LED and the photodiode, while its spectrum-temperature sensitivity is mostly determined by the InGaP bandgap narrowing. Moreover, the operating conditions of the series-connected LED and photodiode within the upconversion device circuit eventually determine the overall current flowing through the LED and the emission intensity. Figure 2h plots the current–voltage characteristics of the LED and the photodiode at temperatures from 25°C to 90°C . Due to the bandgap narrowing of GaAs and InGaP (Fig. S2), both the photodiode open-circuit voltage and the LED turn-on voltage decrease upon heating. In such an upconversion device circuit (Fig. 1a), both the current and the voltage of the LED and the photodiode should match each other. Therefore, the intersection points of the current–voltage curves in Fig. 2h define the working conditions of both devices, which are plotted in Fig. 2i. It is noted that the intersection points of the current–voltage curves are also dependent on other factors, including the device structure as well as the excitation conditions. As shown in Fig. S7, temperature-dependent intensity sensitivities can be tuned by changing the excitation intensity.

As previously demonstrated^{31,32}, these NIR-to-red upconversion devices exhibit ultrafast PL dynamics with a decay lifetime of $\sim 20 \text{ ns}$, enabling them to record temporally resolved thermal information. In addition, these devices can be lithographically patterned to form large arrays of various geometries with a high yield, which also makes spatially resolved temperature mapping feasible.

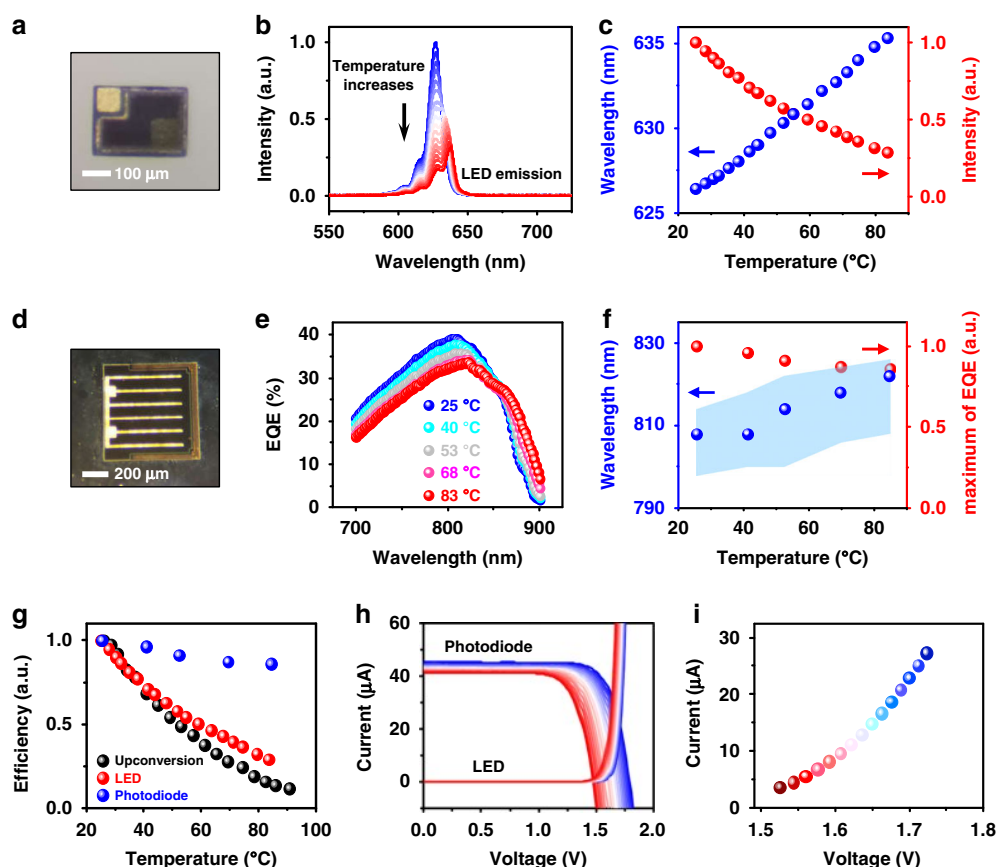


Fig. 2 Thermal behaviors of individual InGaP LED and GaAs photodiode. **a** Micrograph of an InGaP LED. **b** Electroluminescence (EL) spectra of the InGaP LED at varied temperatures (25–90 °C), with an injected forward current of 20 μA . **c** EL intensity changes (red dots) and peak wavelength shifts (blue dots) for the InGaP LED at different temperatures. **d** Micrograph of a double junction GaAs photodiode. **e** External quantum efficiency (EQE) spectra of the GaAs photodiode at different temperatures. **f** Peak absorption intensity changes (red dot) and peak wavelength shifts (blue dot) of the GaAs photodiode at different temperatures. The shaded blue region is the wavelength range where the absorption intensity is above 98% of the peak. **g** Summary of efficiency results, including PL of the upconversion device, EL of the LED, and EQE of the photodiode at varied temperatures (25–90 °C). **h** Current–voltage curves of the InGaP LED and the GaAs photodiode (under irradiance 40 mW cm^{-2} , 810 nm) at varied temperatures from 25 °C (blue) to 90 °C (red). **i** Values of current and voltage at the intersection points in **h**, indicating the corresponding working conditions of the optoelectronic upconversion device

Figure 3a illustrates a fully fabricated device, with PL mappings taken by a microscopic camera at various temperatures (mappings at more temperatures are shown in Fig. S8). Figure 3b plots the corresponding relation of PL intensity (measured by counting the averaged number of captured photons with an imaging sensor) and temperature, and the trend is similar to that obtained by a spectrometer (Fig. 1e). Figure 3c, d, and S9 demonstrate the dynamic response of the device during a cyclic heating/cooling process (between 26 °C and 38 °C) or a step rise at various temperatures. It should be noted that the long rise and decay time (>10 s) is mainly caused by the slow response of the electric heating plate, rather than the PL response of the device. In an environment with well controlled temperatures, the device presents a stable signal output, and PL signals are fully reversible under cyclic

heating/cooling. Furthermore, we form an array of devices (size $\sim 2 \text{ cm}^2$, with ~ 1500 devices) to showcase the capability of spatially resolved thermal sensing (Fig. 3e and Movie S1). At room temperature, the device array presents a uniform red emission under NIR excitation. A hot airflow blows on the sample, disturbs and eventually extinguishes the emission when the surface temperature is above ~ 95 °C. The visualized thermal maps can be quantified based on the intensity–temperature calibration obtained in Fig. 3b. In terms of spatial resolution, the performance of the current array is determined by the device pitch ($\sim 300 \mu\text{m}$), which can be further reduced to several micrometers by optimized lithographical processes. Since the technique records PL emissions at visible wavelengths (~ 625 nm), it potentially owns a spatial resolution much higher than conventional thermal

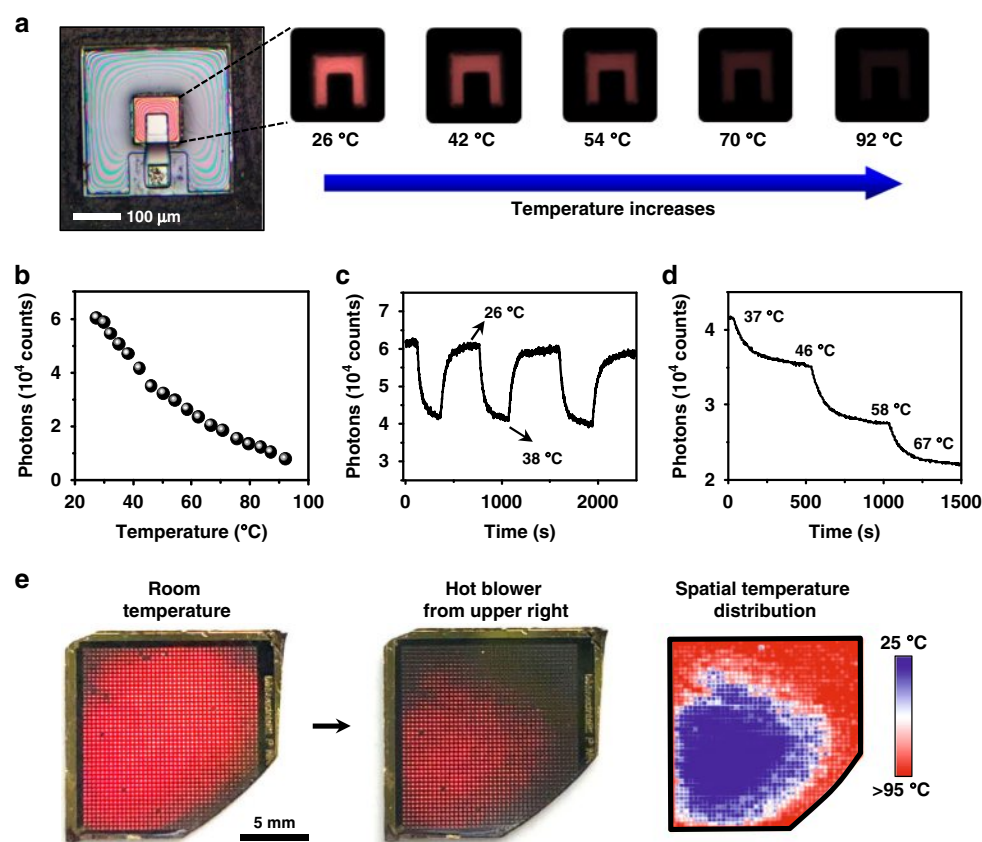


Fig. 3 Dynamic thermal sensing and mapping based on the upconversion devices. **a** Microscopic images show PL emissions of an optoelectronic upconversion device, with the intensity changing with the temperature from 26 °C to 92 °C. **b** Relation of PL intensity versus temperature. **c** Cycled temperature test of the device repeatedly changes from 26 °C to 38 °C. **d** PL intensity of the device responding to step-tuned temperature changes. **e** Spatially resolved PL responses of a device array at room temperature (left) and under nonuniform heating (middle). Right: the corresponding temperature mapping

imagers, which is based on mid-IR or far-IR absorbing materials and ultimately limited by the wavelength of blackbody radiation (10–20 μm at room temperature).

The upconversion device can further be integrated with fiber optics to form light-guided thermal sensors. Epitaxial lift-off and transfer printing techniques produce thin-film, freestanding devices mounting on tips of quartz fibers (Fig. 4a, S10, and S11). Different from free space detectors, such integrated fiber sensors can be interfaced with standard optical setups and transmit all signals within the fibers. Figure 4b outlines the setup established for fiber-based temperature sensing, with a NIR excitation LED ($\sim 810\text{ nm}$) and a spectrometer connected to the two branches of a Y-shaped fiber terminated by our upconversion fiber. In parallel, the optical system can employ a standard thermocouple for calibration and comparison. The encapsulated device on the fiber tip exhibit desirable stability when immersed in the phosphatebuffered saline solution (up to 30 days at room temperature), as well as ideal mechanical stability (Fig. S12). Such a fiber-coupled,

portable system can be conveniently applied for biomedical applications, for example, monitoring the exhalation behavior closed to the mouth of a human, as a proof-of-concept demonstration (Fig. 4d). With the correlation between the PL intensity/peak wavelength and temperature (Fig. S13) established from the calibration with the thermal couple, the fiber sensor can monitor the change of exhaled temperature with time. As shown in Fig. 4e, S13, S14, and Movie S2, both curves match well with the results obtained by a colocalized thermocouple, showing determination coefficients $R^2 = 0.90$.

The fiber-coupled device can also monitor the temperature fluctuations in the deep brain. While magnetic resonance based non-invasive measurements of the deep brain temperature are possible^{38,39}, the accuracy and system complexity still limit their broad applications. Complementary with tethered electrical sensors, such an optical-based technique is more suitable for use in environments with strong electromagnetic interferences, and in particular, capable of obtaining signals during magnetic resonance

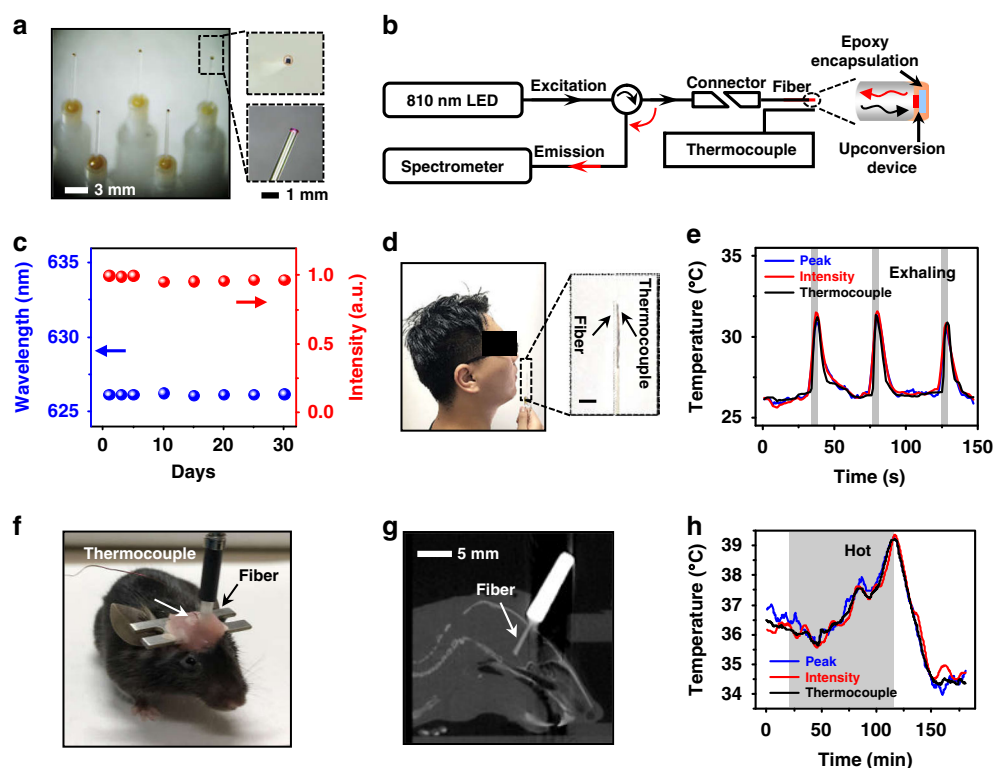


Fig. 4 Optoelectronic upconversion devices integrated with fiber optics for in vivo temperature sensing. **a** Photographs of upconversion devices transferred on the tips of silica fibers (diameter ~600 μm). Enlarged boxes present a zoomed-in view of the fiber tip with a red-emitting device excited by the coupled near-infrared light. **b** Schematic illustration of the temperature sensing setup for spectral analysis, mainly including an 810 nm LED source, a spectrometer, and a Y-shaped fiber, as well as a thermocouple for temperature calibration. **c** Chronic PL stability of the encapsulated fiber sensor immersed in PBS for different times at room temperature (~25 $^{\circ}\text{C}$), in which both the peak wavelength and PL intensity are recorded. **d** Photograph of the exhalation temperature detection with the fiber sensor. **e** Dynamic temperature signals during cycled exhaling activities obtained by the fiber sensor based on the emission peak wavelength shifts and PL intensity changes, compared with results simultaneously recorded by the thermocouple. The gray regions represent actions of exhaling. **f** Photograph of a behaving mouse with a fiber sensor and a thermocouple implanted into the brain for temperature sensing. **g** Sagittal CT reconstruction of a slice, indicating the location of the implanted fiber. **h** Dynamic temperature signals obtained in the mouse brain by the fiber sensor based on the emission peak wavelength shifts and PL intensity changes, compared with results simultaneously recorded by the thermocouple. The shaded gray region represents the time period when the mouse is placed in a hot environment at around 40 $^{\circ}\text{C}$.

imaging (MRI). As a consequence, some commercially available fiber optic temperature sensors^{40,41} based on the temperature-dependent optical properties, e.g., the bandgap of a GaAs crystal material, as the thermal transduction mechanisms have been put into practice⁴². Different from these semiconductor-based sensors via downconversion photoluminescence, our thin-film devices leverage the thermal behaviors of semiconductor bandgaps and diode junctions, which potentially provide improved sensitivities, and the upconversion mechanism minimizes tissue attenuation and autofluorescence associated with the use of visible excitation sources. Figure 4f shows a behaving mouse with a fiber sensor as well as a thermocouple inserted in the same brain region via standard stereotaxic surgery (details provided in methods). The reconstructed x-ray computed tomography (CT) images in Fig. 4g reveal that the fiber tip is located in the hypothalamus region. To minimize the

thermal effect of the excitation source, a pulsed NIR light (810 nm, power 1 mW, frequency 0.1 Hz, pulse width 3 s) is applied to illuminate the upconversion device. We place the mouse in a temperature-controlled enclosure and dynamically record the optical response of the implanted fiber sensor while changing the ambient temperature. Similarly, temperature results can be extracted from both the PL intensity and peak wavelength variations. Figure 4h, S13, and S14 present the brain temperature simultaneously recorded by the fiber and the thermocouple in a period of 3 h, and the results indicate that these optical and electrical readouts are in good accordance with a determination coefficient $R^2 > 0.97$. The brain temperature increases when the mouse is in a hot environment (~40 $^{\circ}\text{C}$), and then drops to ~34 $^{\circ}\text{C}$ when the heat is turned off, due to the heat dysregulation response^{43,44}. Therefore, this fiber-based thermal sensor can be exploited together with other neural modulation and

interrogation methodologies like optogenetics and fluorescence photometry^{7,45,46}, making it feasible to probe the local thermal condition of a specific brain region.

Discussion

In summary, here we present an optical thermometer comprising integrated optoelectronic devices for photon upconversion, with an intensity-temperature sensitivity of $1.5\% \text{ } ^\circ\text{C}^{-1}$ and a large spectral shift of $0.18 \text{ nm } ^\circ\text{C}^{-1}$, in the range of $20\text{--}90 \text{ } ^\circ\text{C}$. Compared to other upconversion materials like lanthanide nanoparticles, dyes, and quantum dots, our device provides an alternative approach for temperature sensing, featuring high sensitivities and low-power excitation. Based on similar semiconductor materials and architectures, large-area device arrays with a wafer-level scale and pitches of a few micrometers can be readily archived for thermal mapping with a high resolution. The MRI-compatible, implantable sensors combined with fiber optics offer both research and clinical significance, with a potential for localized temperature monitoring in the deep body. One limitation of the current device design is its red emission ($\sim 625 \text{ nm}$), which is not within the biological transparency window. Future design can involve semiconductors both absorption and emission at longer wavelengths. Overall, these materials and device concepts establish a power tool set with vast applications in the environment and healthcare.

Materials and methods

Device fabrication

Details about the structure and fabrication processes of the optoelectronic upconversion devices can be found in our previous work^{31,32}. Via metal-organic chemical vapor deposition (MOCVD), the InGaP red LED and the double junction GaAs photodiode are grown on a GaAs substrate, with an $\text{Al}_{0.95}\text{Ga}_{0.05}\text{As}$ sacrificial layer between the device layers and the GaAs substrate. The device geometry is lithographically patterned by selective wet etching and metallization. Thin-film, freestanding devices are formed by eliminating the sacrificial layer, and fully released devices are transferred printed onto the thermal release tape. The devices are detached from the heat release tape (3198 M, Semiconductor Equipment Corp.) by heating the tape to $120 \text{ } ^\circ\text{C}$. Pick up the detached device with the epoxy (SU8-3005) coated fiber tip, followed by encapsulation with $\sim 20 \text{ }\mu\text{m}$ thick polydimethylsiloxane (PDMS, Sylgard-184, Dow Corning, base: curing agent ratio = 10:1 w/w, cured at $80 \text{ } ^\circ\text{C}$ for 2 h) and then $\sim 10 \text{ }\mu\text{m}$ thick parylene via chemical vapor deposition (CVD).

Device characterization

Devices photographs are taken with an Olympus IX53 microscope equipped with a Xenon arc lamp, in which the excitation light and the emission light pass through a set of

fluorescence filters (EX ET800/60, BS T700spxr-UF1, EM ET650sp, Chroma Tech. Corp.). The PL emission is collected by an Andor Zyla 4.2Plus CMOS camera (an area of $\sim 20 \text{ }\mu\text{m}^2$ is chosen, acquisition time 20 ms) or a spectrometer (HR2000+, Ocean Optics). Samples are placed on a ceramic electric heating plate for temperature control, which is calibrated by a thermocouple. The current–voltage characteristics of devices are measured with a Keithley 2400 source meter. The EQE spectra of photodiodes are collected by a standard system (QEX10, PV Measurement). A standard thermocouple (YET-620) with a T-type microprobe is used for temperature reference and system calibration.

Animal studies

All animal procedures are approved by the Institutional Animal Care and Use Committee (IACUC) at Tsinghua University. Adult male C57BL/6 J mice (8–12 weeks) are purchased from the Vital River Laboratory Animal Technology (Beijing, China), and are used and housed under standard conditions in groups (3–5 mice per cage).

Following anesthesia with an intraperitoneal injection of 0.5% sodium pentobarbital (10 mL kg^{-1}), the scalp is shaved and the mice are placed in a stereotaxic frame. A hole with a diameter of $\sim 800 \text{ }\mu\text{m}$ is drilled in the implantation site on the skull, the fiber sensor is slowly inserted into the hypothalamus (AP: 0.5 mm , ML: 0.5 mm , DV: -4.8 mm), and then the fiber sensor is secured to the skull by dental cement.

Acknowledgements

National Natural Science Foundation of China (NSFC) (62005016, 61874064); Tsinghua University Initiative Scientific Research Program; Beijing Municipal Natural Science Foundation (4202032); EnSan Frontier Innovation Foundation (2022003). The authors also acknowledge characterization work supported by Beijing Institute of Technology Analysis & Testing Center and Tsinghua Nanofabrication Technology Center.

Author details

¹Beijing Engineering Research Center of Mixed Reality and Advanced Display, School of Optics and Photonics, Beijing Institute of Technology, Beijing 100081, China. ²Department of Electronic Engineering, Beijing National Research Center for Information Science and Technology, Institute for Precision Medicine, Center for Flexible Electronics Technology, and IDG/McGovern Institute for Brain Research, Tsinghua University, Beijing 100084, China. ³School of Materials Science and Engineering, Tsinghua University, Beijing 100084, China

Author contributions

H.D. and X.S. developed the concepts. H.D., G.L., J.C., Z.C., Z.S., Y.X., G.T., and Y.P. performed simulation, material design, fabrication, and characterization. H.D., X.C., J.C., X.F., and X.S. designed and performed biological experiments. H.D., L.Y., J.Y., Y.W., and X.S. provided tools and supervised the research. H.D. and X.S. wrote the paper in consultation with other authors.

Conflict of interest

The authors declare no competing interests.

Supplementary information The online version contains supplementary material available at <https://doi.org/10.1038/s41377-022-00825-5>.

Received: 11 February 2022 Revised: 9 April 2022 Accepted: 27 April 2022
Published online: 07 May 2022

References

- Childs, P. R. N., Greenwood, J. R. & Long, C. A. Review of temperature measurement. *Rev. Sci. Instrum.* **71**, 2959–2978 (2000).
- Oh, Y. S. et al. Battery-free, wireless soft sensors for continuous multi-site measurements of pressure and temperature from patients at risk for pressure injuries. *Nat. Commun.* **12**, 5008 (2021).
- Liao, J. & Yang, L. Optical whispering-gallery mode barcodes for high-precision and wide-range temperature measurements. *Light: Sci. Appl.* **10**, 32 (2021).
- Palmer, T. & Stevens, B. The scientific challenge of understanding and estimating climate change. *Proc. Natl Acad. Sci. USA* **116**, 24390–24395 (2019).
- Duhr, S. & Braun, D. Why molecules move along a temperature gradient. *Proc. Natl Acad. Sci. USA* **103**, 19678–19682 (2006).
- Zhu, X. J. et al. Temperature-feedback upconversion nanocomposite for accurate photothermal therapy at facile temperature. *Nat. Commun.* **7**, 10437 (2016).
- Owen, S. F., Liu, M. H. & Kreitzer, A. C. Thermal constraints on in vivo optogenetic manipulations. *Nat. Neurosci.* **22**, 1061–1065 (2019).
- Shin, J. et al. Bioresorbable optical sensor systems for monitoring of intracranial pressure and temperature. *Sci. Adv.* **5**, eaaw1899 (2019).
- Wang, X. D., Wolfbeis, O. S. & Meier, R. J. Luminescent probes and sensors for temperature. *Chem. Soc. Rev.* **42**, 7834–7869 (2013).
- Del Rosal, B. et al. In vivo luminescence nanothermometry: from materials to applications. *Adv. Optical Mater.* **5**, 1600508 (2017).
- Zhou, J. et al. Advances and challenges for fluorescence nanothermometry. *Nat. Methods* **17**, 967–980 (2020).
- Dramicanin, M. D. Trends in luminescence thermometry. *J. Appl. Phys.* **128**, 040902 (2020).
- Vollmer, M. & Möllmann, K. P. *Infrared Thermal Imaging: Fundamentals, Research and Applications*. (John Wiley & Sons, Weinheim, 2010).
- Rogalski, A. History of infrared detectors. *Opto-Electron. Rev.* **20**, 279–308 (2012).
- Tamaoki, N. Cholesteric liquid crystals for color information technology. *Adv. Mater.* **13**, 1135–1147 (2001).
- Coles, H. J. & Pivnenko, M. N. Liquid crystal ‘blue phases’ with a wide temperature range. *Nature* **436**, 997–1000 (2005).
- Gao, L. et al. Epidermal photonic devices for quantitative imaging of temperature and thermal transport characteristics of the skin. *Nat. Commun.* **5**, 4938 (2014).
- Liu, X. L. et al. Fast wide-field upconversion luminescence lifetime thermometry enabled by single-shot compressed ultrahigh-speed imaging. *Nat. Commun.* **12**, 6401 (2021).
- Brites, C. D. S., Balabhadra, S. & Carlos, L. D. Lanthanide-based thermometers: at the cutting-edge of luminescence thermometry. *Adv. Optical Mater.* **7**, 1801239 (2019).
- Cortese, A. J. et al. Microscopic sensors using optical wireless integrated circuits. *Proc. Natl Acad. Sci. USA* **117**, 9173–9179 (2020).
- Fedotov, I. V. et al. All-optical brain thermometry in freely moving animals. *ACS Photonics* **7**, 3353–3360 (2020).
- Weissleder, R. A clearer vision for in vivo imaging. *Nat. Biotechnol.* **19**, 316–317 (2001).
- Guo, J. J. et al. Stretchable and temperature-sensitive polymer optical fibers for wearable health monitoring. *Adv. Funct. Mater.* **29**, 1902898 (2019).
- Zhang, F. *Photon Upconversion Nanomaterials*. 416 (Springer, Berlin, 2015).
- Xu, M. et al. Ratiometric nanothermometer in vivo based on triplet sensitized upconversion. *Nat. Commun.* **9**, 2698 (2018).
- Chen, G. Y. et al. Upconversion nanoparticles: design, nanochemistry, and applications in theranostics. *Chem. Rev.* **114**, 5161–5214 (2014).
- Lyapin, A. A. et al. Infrared-to-visible upconversion luminescence in $\text{SrF}_2\text{:Er}$ powders upon excitation of the $^4\text{I}_{13/2}$ level. *Optical Mater. Express* **8**, 1863–1869 (2018).
- Zhou, J. et al. A new generation of dual-mode optical thermometry based on $\text{ZrO}_2\text{:Eu}^{3+}$ nanocrystals. *Nanophotonics* **8**, 2347–2358 (2019).
- Brites, C. D. S. et al. Instantaneous ballistic velocity of suspended Brownian nanocrystals measured by upconversion nanothermometry. *Nat. Nanotechnol.* **11**, 851–856 (2016).
- Yang, Y. et al. Semiconductor infrared up-conversion devices. *Prog. Quantum Electron.* **35**, 77–108 (2011).
- Ding, H. et al. Microscale optoelectronic infrared-to-visible upconversion devices and their use as injectable light sources. *Proc. Natl Acad. Sci. USA* **115**, 6632–6637 (2018).
- Shi, Z. et al. Ultrafast and low-power optoelectronic infrared-to-visible upconversion devices. *Photonics Res.* **7**, 1161–1168 (2019).
- Klapoetke, N. C. et al. Independent optical excitation of distinct neural populations. *Nat. Methods* **11**, 338–346 (2014).
- Shockley, W. & Queisser, H. J. Detailed balance limit of efficiency of p - n junction solar cells. *J. Appl. Phys.* **32**, 510–519 (1961).
- Varshni, Y. P. Temperature dependence of the energy gap in semiconductors. *Physica* **34**, 149–154 (1967).
- Vurgaftman, I., Meyer, J. R. & Ram-Mohan, L. R. Band parameters for III–V compound semiconductors and their alloys. *J. Appl. Phys.* **89**, 5815–5875 (2001).
- Ding, H. et al. Power- and spectral-dependent photon-recycling effects in a double-junction gallium arsenide photodiode. *ACS Photonics* **6**, 59–65 (2019).
- Corbett, R., Laptok, A. & Weatherall, P. Noninvasive measurements of human brain temperature using volume-localized proton magnetic resonance spectroscopy. *J. Cereb. Blood Flow. Metab.* **17**, 363–369 (1997).
- Sung, D. et al. Personalized predictions and non-invasive imaging of human brain temperature. *Commun. Phys.* **4**, 68 (2021).
- Weidmann Technologies Deutschland GmbH. at <https://weidmann-optocon.com/products/fiber-sensors-probes/>.
- Opsens Inc. OTG-M170. at <https://opsensmedical.com/products/oem-lifescience-solutions/fiber-optic-temperature-sensors/otg-m170/>.
- Kyuma, K. et al. Fiber-optic instrument for temperature measurement. *IEEE Trans. Microw. Theory Tech.* **30**, 522–525 (1982).
- Deuis, J. R., Dvorakova, L. S. & Vetter, I. Methods used to evaluate pain behaviors in rodents. *Front. Mol. Neurosci.* **10**, 284 (2017).
- Miyamoto, K. et al. A novel mouse model of heatstroke accounting for ambient temperature and relative humidity. *J. Intensive Care* **9**, 35 (2021).
- Vogt, N. Optogenetics turns up the heat. *Nat. Methods* **16**, 681 (2019).
- Meng, C. B. et al. Spectrally resolved fiber photometry for multi-component analysis of brain circuits. *Neuron* **98**, 707–717.e4 (2018).

Supplementary Information for

**An Optoelectronic Thermometer based on Microscale
Infrared-to-Visible Conversion Devices**

He Ding^{1,*}, Guoqing Lv¹, Xue Cai², Junyu Chen², Ziyi Cheng¹, Yanxiu Peng¹, Guo
Tang², Zhao Shi², Yang Xie², Xin Fu³, Lan Yin³, Jian Yang¹, Yongtian Wang¹, Xing
Sheng^{2,*}

¹Beijing Engineering Research Center of Mixed Reality and Advanced Display,
School of Optics and Photonics, Beijing Institute of Technology, Beijing, China

²Department of Electronic Engineering, Beijing National Research Center for
Information Science and Technology, Institute for Precision Medicine, Center for
Flexible Electronics Technology, and IDG/McGovern Institute for Brain Research,
Tsinghua University, Beijing, China

³School of Materials Science and Engineering, Tsinghua University, Beijing, China

* Corresponding to: heding@bit.edu.cn; xingsheng@tsinghua.edu.cn

Calculations of the emission peak wavelength and intensity the upconversion device as a function of the temperature

The optical and electrical properties of semiconductor materials are highly susceptible to temperature, so the spectral response of optoelectronic upconversion devices can be determined by temperature changes (1–3).

As the temperature (T , in unit Kelvin) increases, energy band gaps (E_g) of the semiconductors (InGaP and GaAs) decreases, based on the empirical Varshni expression (3):

$$E_g(T) = E_g(0) - \frac{\alpha T^2}{T + \beta} \quad (1)$$

where $E_g(0)$ is the energy bandgap at $T = 0$ K, $E_{g_InGaP}(0) = 2.07$ eV, $E_{g_GaAs}(0) = 1.52$ eV, α and β are fitting parameters ($\alpha_{InGaP} = 4.8 \times 10^{-4} \text{ K}^{-1}$, $\beta_{InGaP} = 200$ K; $\alpha_{GaAs} = 5.4 \times 10^{-4} \text{ K}^{-1}$, $\beta_{GaAs} = 204$ K) from the literature (3, 4). Data are plotted in Figure S4 (blue curve).

The emission peak wavelength (λ) of the InGaP LED can be calculated as a function of the temperature:

$$\lambda(T) = \frac{hc}{E_g(T)} \quad (2)$$

where h is Planck's constant, c is the speed of light. Based on Eq.(2), we can calculate the wavelength vs. temperature plot in Figure 1e.

Based on the detailed balance theory (2), the output current from the GaAs photodiode I_{PD} is equal to the difference between generated carriers and recombined carriers:

$$I_{PD} = I_{ph} + I_{th} - I_{rad} - I_{nrad} \quad (3)$$

where I_{ph} is the photogenerated current and derived from the excitation light ($\sim 40 \text{ mW cm}^{-2}$), I_{th} is the absorbed thermal radiation from the environment, I_{rad} is the radiative current, and I_{nrad} is the non-radiative current.

Similarly, the input current for the LED is mainly converted to the radiative recombination and non-radiative recombination process.

$$I_{LED} = -I_{th} + I_{rad} + I_{nrad} \quad (4)$$

For both the GaAs photodiode and the InGaP LED, the absorbed thermal radiative current is defined as:

$$I_{th} = \frac{2\pi(n^2 + 1)qkTS}{h^3c^2} E_g^2 \exp\left(-\frac{E_g}{kT}\right) \quad (5)$$

where k is Boltzmann's constant, n is the refractive index, and S is the surface area of the device. In the temperature range of our interest (20–100 °C), the thermal currents are around $1 \times 10^{-26} \text{ A m}^{-2}$ (for InGaP) and $1 \times 10^{-18} \text{ A m}^{-2}$ (for GaAs), much smaller than the photocurrents ($\sim 1 \text{ A m}^{-2}$) under excitation. Therefore, the effect of thermal currents can be neglected in such an integrated device.

The radiative current is dependent on the voltage (V) and defined as:

$$I_{rad} = I_{th} \exp\left(\frac{qV}{kT}\right) \quad (6)$$

The radiative and absorption efficiencies of the LED and double junction GaAs photodiode are assumed to linearly drop from 100% to 30% and from 100% to 90%, respectively, from 25 °C to 100 °C, as shown in Figures 2c and 2f. The conversion efficiency (η) is highly dependent on the temperature changes, and the major fraction

of the carriers contribute to non-radiative recombination and carrier leakage, resulting in low efficiency (5). Taking these conversion efficiencies (η) of the diode from the experimental results, in which the I_{nard} is defined as:

$$I_{\text{nard}} = \frac{I_{\text{rad}}}{\eta} - I_{\text{rad}} \quad (7)$$

Thus the I_{LED} and I_{PD} can be summarized as:

$$\begin{aligned} I_{\text{LED}} &= -I_{\text{th}} + I_{\text{rad}} + I_{\text{nard}} \\ &= \frac{2\pi(n^2+1)qkTS}{h^3c^2} \left(E_{\text{g_InGaP}}(0) - \frac{\alpha_{\text{InGaP}}T^2}{T + \beta_{\text{InGaP}}} \right)^2 \exp \left(-\frac{E_{\text{g_InGaP}}(0) - \frac{\alpha_{\text{InGaP}}T^2}{T + \beta_{\text{InGaP}}}}{kT} \right) \left(-1 + \frac{\exp\left(\frac{qV}{kT}\right)}{\eta_{\text{LED}}} \right) \end{aligned} \quad (8)$$

$$\begin{aligned} I_{\text{PD}} &= I_{\text{ph}} + I_{\text{th}} - I_{\text{rad}} - I_{\text{nard}} \\ &= I_{\text{ph}} + \frac{2\pi(n^2+1)qkTS}{h^3c^2} \left(E_{\text{g_GaAs}}(0) - \frac{\alpha_{\text{GaAs}}T^2}{T + \beta_{\text{GaAs}}} \right)^2 \exp \left(-\frac{E_{\text{g_GaAs}}(0) - \frac{\alpha_{\text{GaAs}}T^2}{T + \beta_{\text{GaAs}}}}{kT} \right) \left(1 - \frac{\exp\left(\frac{qV}{kT}\right)}{\eta_{\text{PD}}} \right) \end{aligned} \quad (9)$$

I_{LED} vs. V and I_{PD} vs. V under different illumination conditions are plotted in Figures 2h and S7a.

In the optoelectronic upconversion device, the double junction GaAs photodiode structure is connected in series to the InGaP LED structure. Under illumination, the current and voltage of the integrated design should satisfy:

$$\begin{cases} I_{\text{LED}} = I_{\text{PD}} \\ V_{\text{LED}} = V_{\text{PD}} - V_{\text{f}} - I_{\text{LED}}R_{\text{LED}} - I_{\text{PD}}R_{\text{PD}} \end{cases} \quad (10)$$

where $V_{\text{f}} = 0.4$ V is a fitting value representing the discrepancy between the theoretical and experimental output voltages of the double junction GaAs photodiode. $R_{\text{LED}} = R_{\text{PD}} = 150$ Ω are series resistances within the device circuit. By solving Eq. (10), we can obtain intensity vs. temperature (red curve) in Figure 1e.

Reference

1. Levinshtein, M., Rumyantsev, S. & Shur, M. Handbook Series on Semiconductor Parameters. (Singapore: World Scientific, 1996).
2. Shockley, W. & Queisser, H. J. Detailed balance limit of efficiency of p - n junction solar cells. *Journal of Applied Physics* **32**, 510-519 (1961).
3. Varshni, Y. P. Temperature dependence of the energy gap in semiconductors. *Physica* **34**, 149-154 (1967).
4. Vurgaftman, I., Meyer, J. R. & Ram-Mohan, L. R. Band parameters for III–V compound semiconductors and their alloys. *Journal of Applied Physics* **89**, 5815-5875 (2001).
5. Meyaard, D. S. *et al.* Temperature dependent efficiency droop in GaInN light-emitting diodes with different current densities. *Applied Physics Letters* **100**, 081106 (2012).

Figure S1

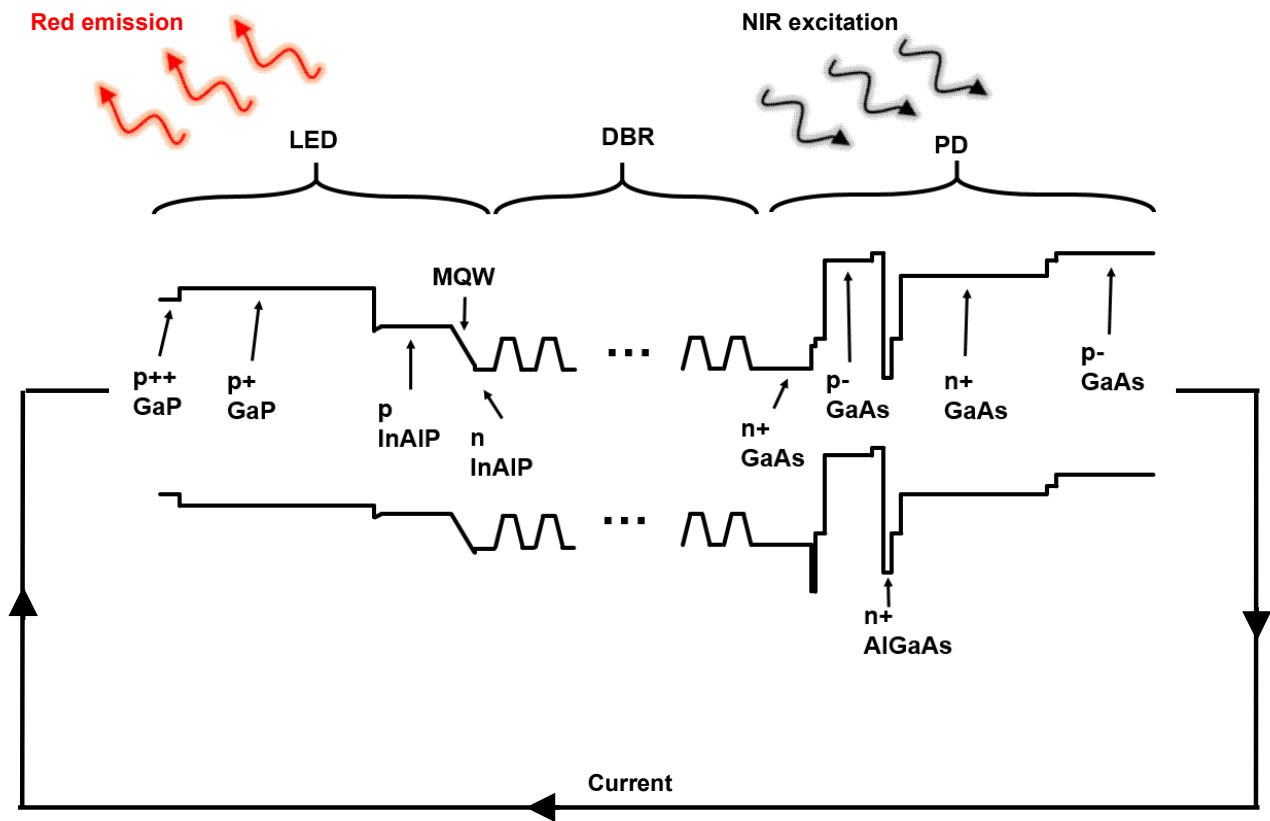


Figure S1. Schematic drawing of the band structure for our optoelectronic upconversion device.

Figure S2

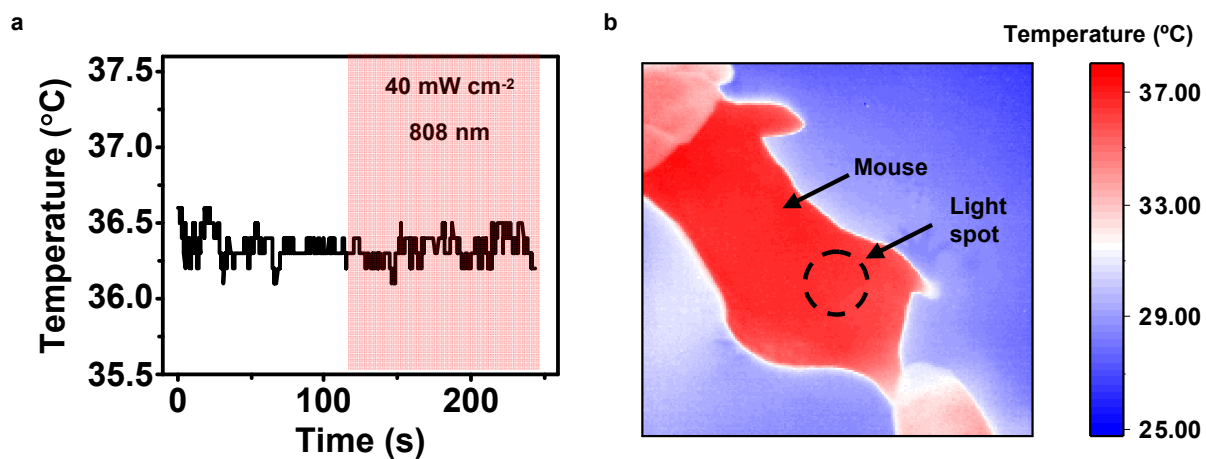


Figure S2. (a) Temperature response of the mouse skin under irradiation at $\sim 40 \text{ mW cm}^{-2}$ at 808 nm. (b) The dashed circle indicates the light spot on the mouse skin.

Figure S3

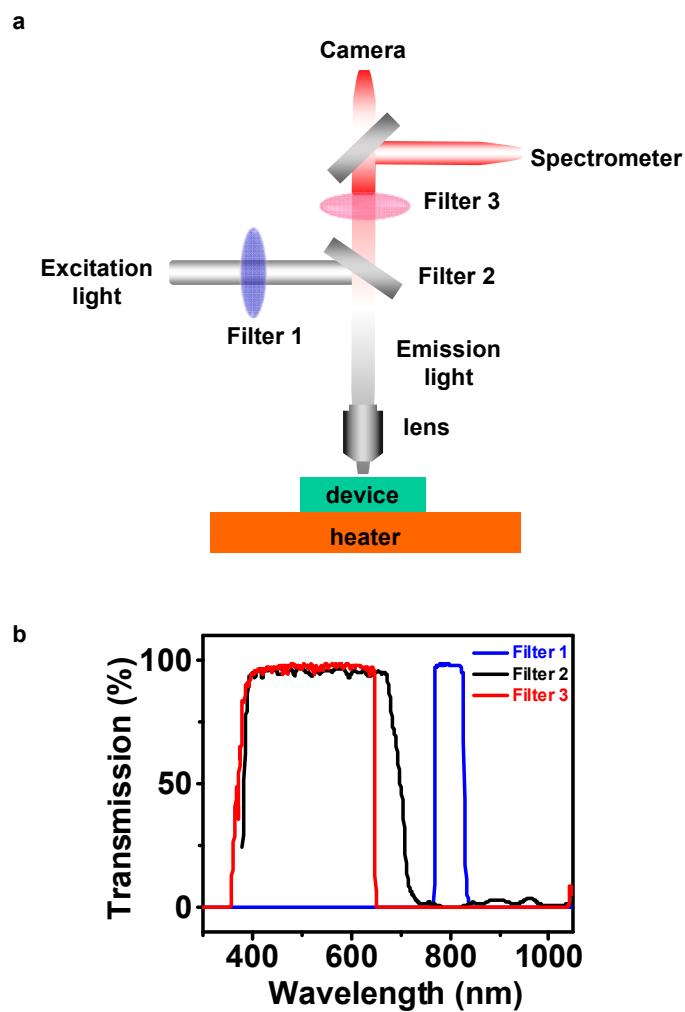


Figure S3. (a) Schematic diagram of the optical setup for temperature sensing based on PL changes of the optoelectronic upconversion device. (b) Optical transmission spectra of fluorescence filter combinations.

Figure S4

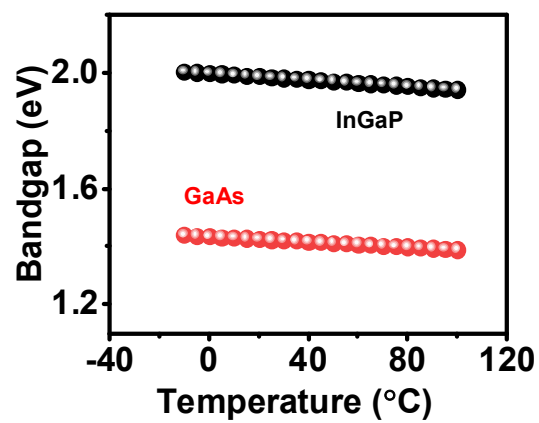


Figure S4. Bandgaps of InGaP and GaAs as a function of the temperature.

Figure S5

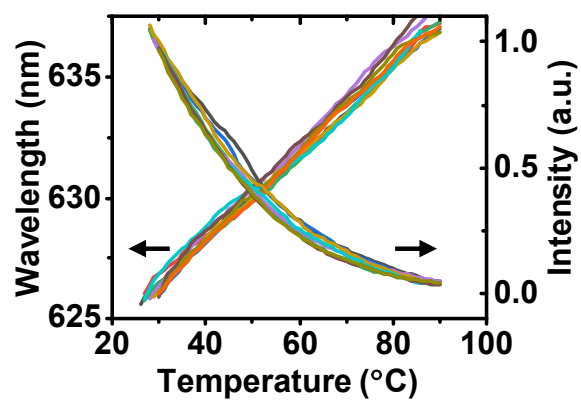


Figure S5. Measured peak wavelength and PL intensity of the upconverted red emission spectra as a function of temperature for a group of 10 different samples.

Figure S6

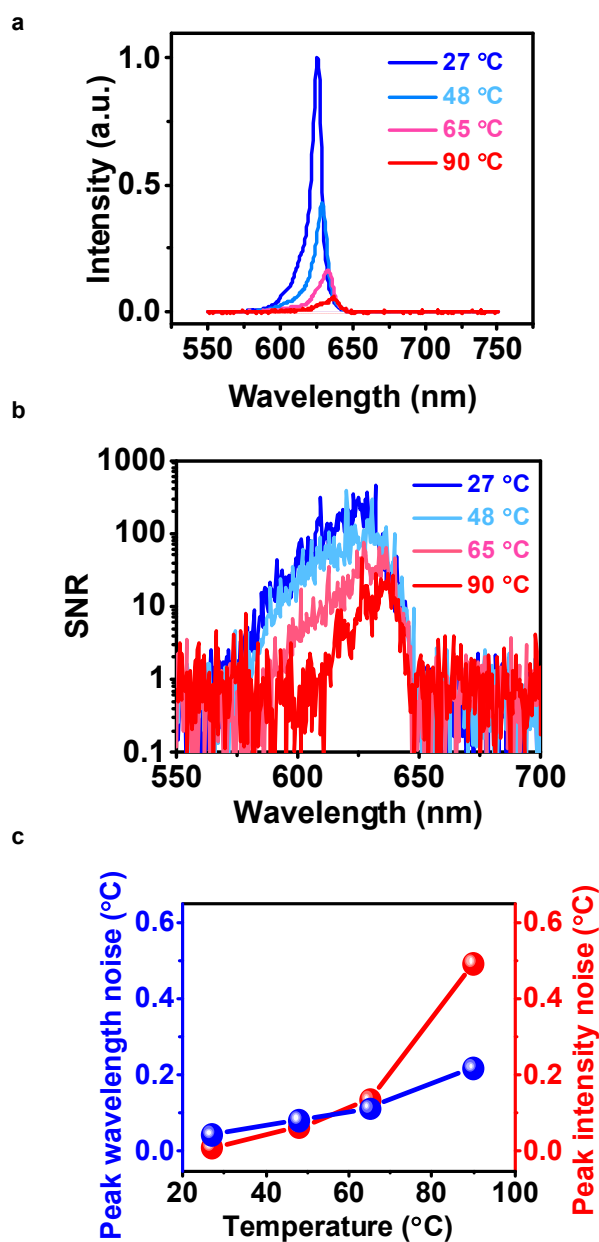


Figure S6. (a) Upconverted emission spectra and (b) signal to noise ratio (SNR) of the optoelectronic upconversion device at the representative temperatures of 27 °C, 48 °C, 65 °C, and 90 °C. (c) The temperature detection accuracy based on peak wavelength shift and intensity changes by noting the equivalency their standard deviation to temperature changes in Figure 2e.

Figure S7

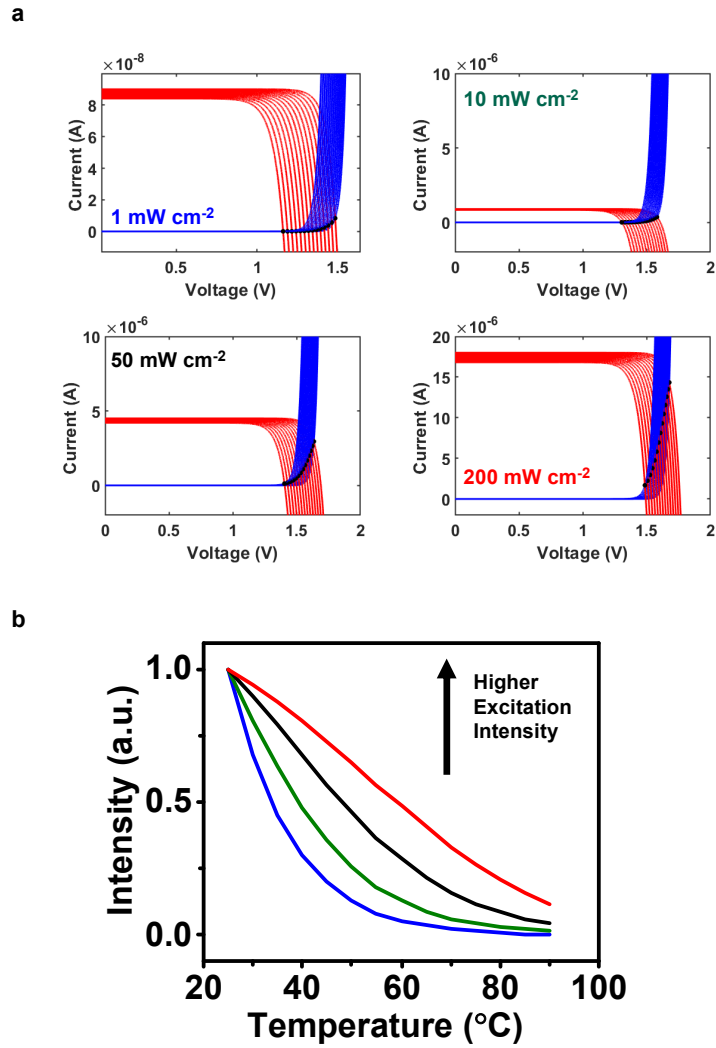


Figure S7. (a) Calculated current–voltage curves of the InGaP LED and the GaAs photodiode structures for the optoelectronic upconversion device at varied temperatures from 25 °C to 90 °C, under the different light intensities from 1 mW cm⁻² to 200 mW cm⁻². (b) Corresponding temperature-dependent intensity changes.

Figure S8

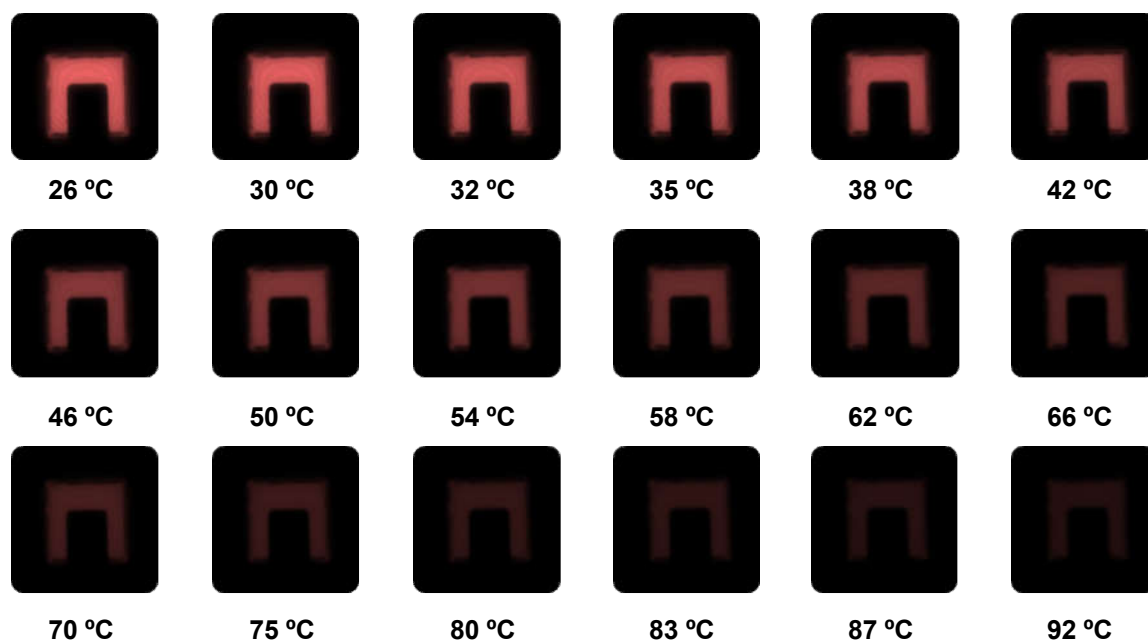


Figure S8. Photographs showing photoluminance intensity changes of an upconversion device, with the temperature increasing from ~26 °C to 92 °C.

Figure S9

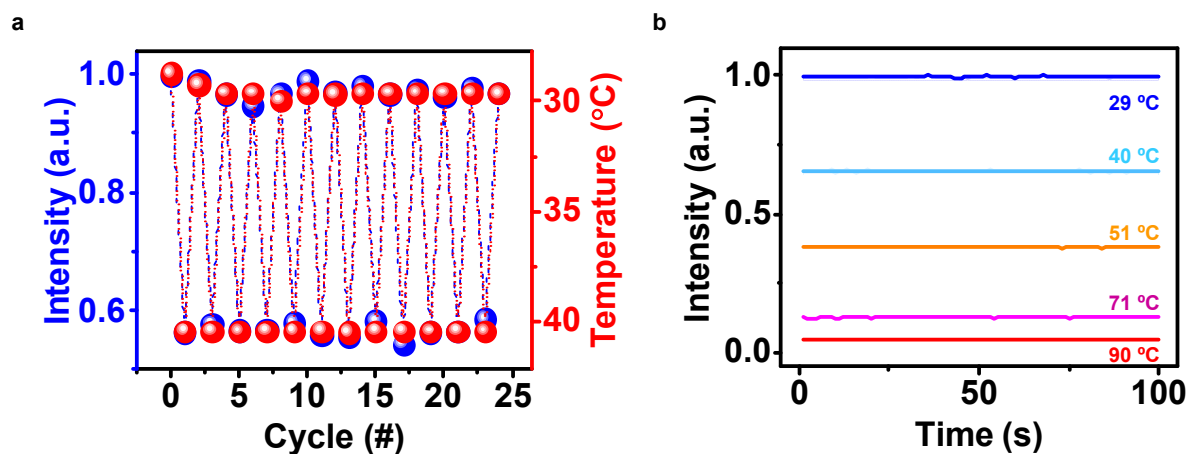


Figure S9. (a) Measured PL intensity and corresponding temperature values under cyclic temperature changes between 28 °C and 41 °C. (b) The stability of the optoelectronic upconversion device at 29 °C, 40 °C, 51 °C, 71 °C, and 90 °C, after the heating plate stabilizes.

Figure S10

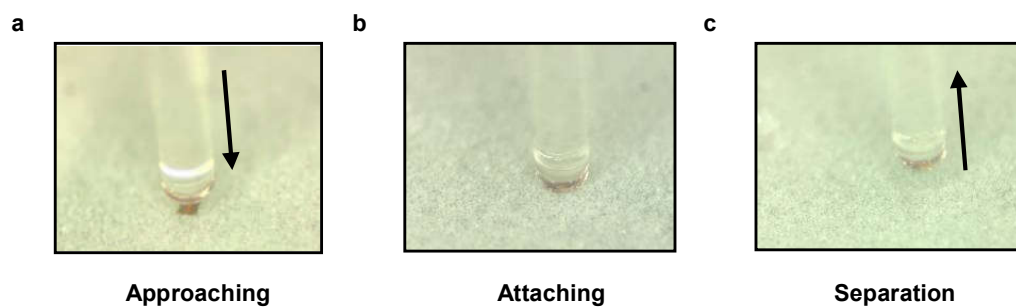


Figure S10. Transfer printing a free-standing microscale upconversion device from a thermal release tape to the optical fiber tip.

Figure S11



Figure S11. Cross-sectional view of the microscope image for the optoelectronic upconversion device integrated on the fiber optics, in which the fiber tip is encapsulated with a bilayer of parylene ($\sim 10\text{ }\mu\text{m}$) and PDMS ($\sim 20\text{ }\mu\text{m}$) .

Figure S12

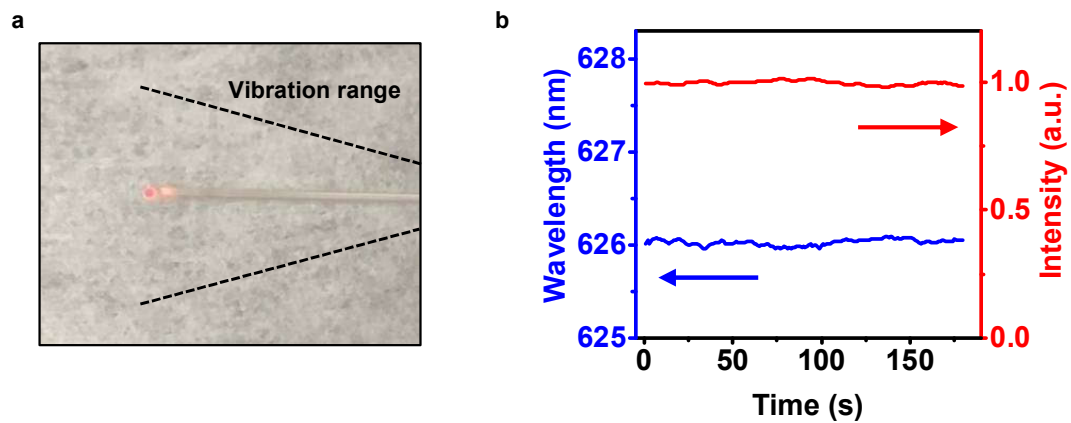


Figure S12. Stability of PL signals recorded from the fiber sensor under vibration conditions, in which the fiber bending angle range is about $\pm 30^\circ$.

Figure S13

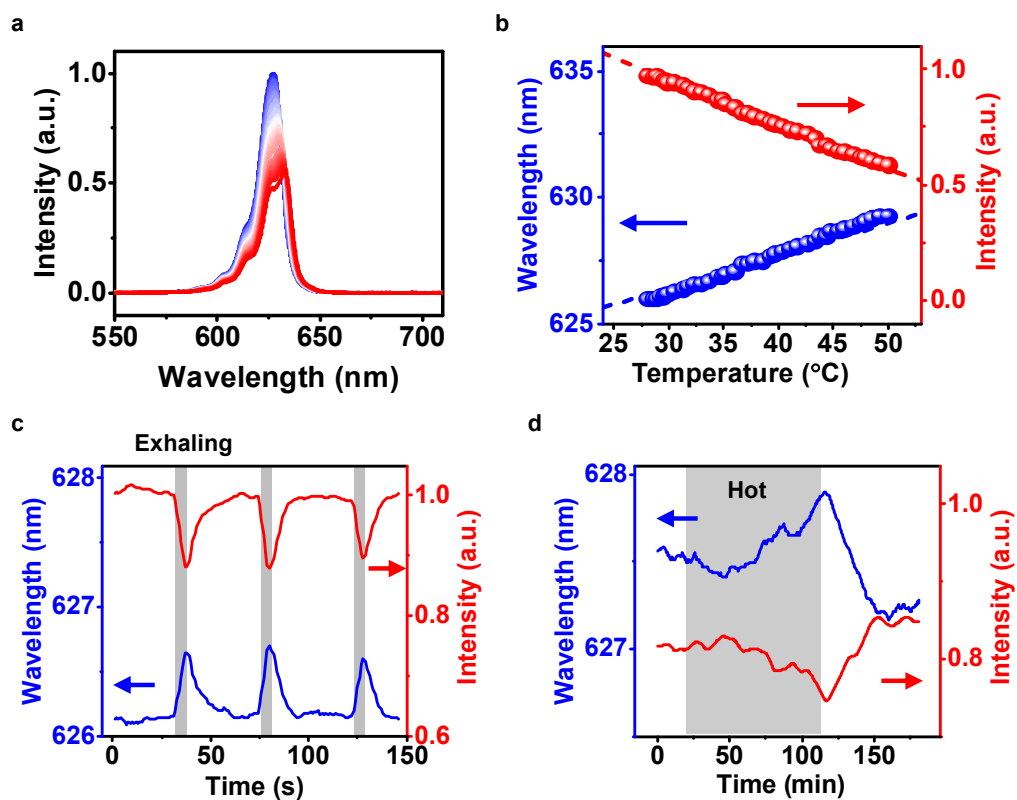


Figure S13. (a) PL emission recorded from the fiber sensor at different temperatures (25–50 °C) in PBS. (b) Calculated (dash line) and measured (dots) emission peak wavelength and PL intensity as a function of temperature. (c) Recorded PL peak wavelength and intensity from the fiber sensor, in response to human respiration. Data are used to plot Figure 4e. (d) Recorded PL peak wavelength and intensity from the fiber sensor, obtained in the mouse brain. Data are used to plot Figure 4h.

Figure S14

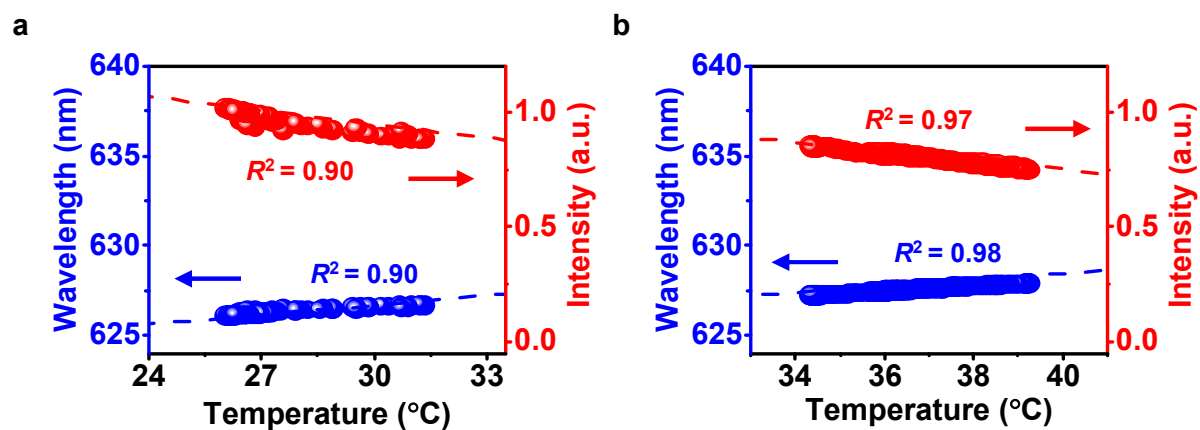
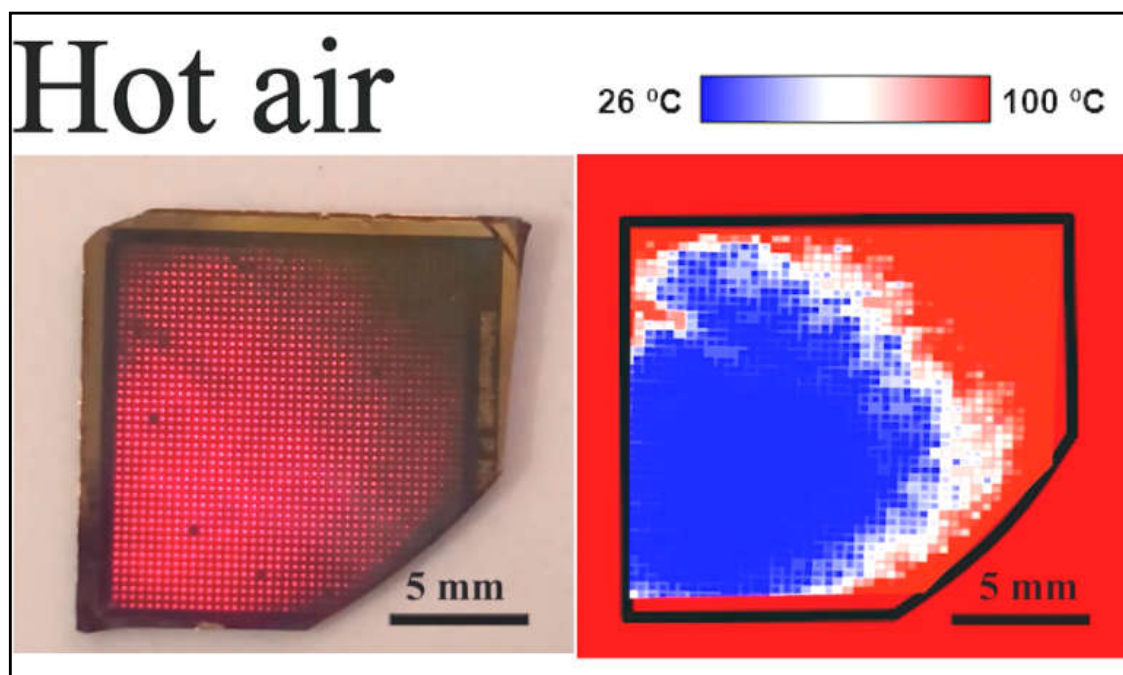


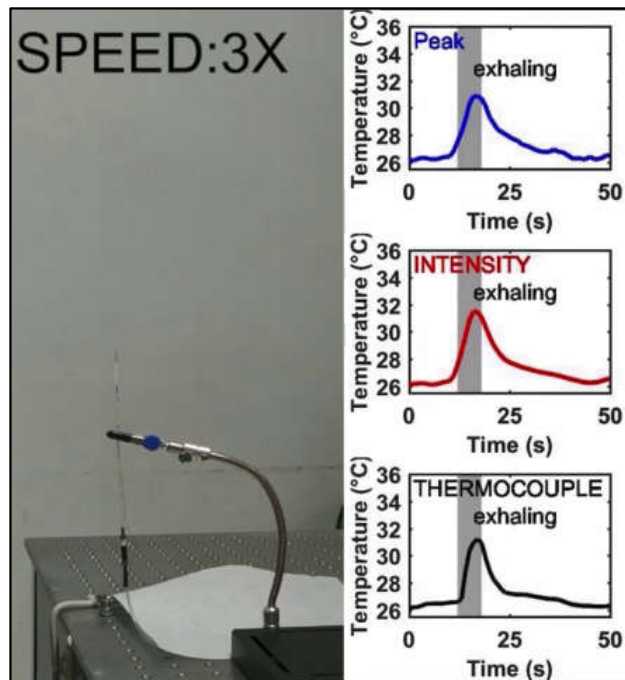
Figure S14. Calculated (dash line) and measured (dots) peak wavelength and PL intensity of the upconverted emission as a function of temperature, corresponding to results in (a) human respiration in Figure 4e and (b) the mouse brain in Figure 4h.

Movie S1



Movie S1. Spatially resolved dynamic PL variations in response to temperature changes based on an optoelectronic upconversion device array.

Movie S2



Movie S2. Dynamic temperature signals during exhaling activities obtained by the fiber sensor based on the emission peak wavelength shifts and PL intensity changes, compared with results simultaneously recorded by the thermocouple.